

A THEORY OF CRITICAL DISTANCES BASED METHODOLOGY FOR THE ANALYSIS OF ENVIRONMENTALLY ASSISTED CRACKING IN STEELS

P. González^{a,*}, S. Cicero^a, B. Arroyo^a, J.A. Álvarez^a.

^aLADICIM (Laboratory of Materials Science and Engineering), University of Cantabria, E.T.S. de Ingenieros de Caminos, Canales y Puertos, Av/Los Castros 44, 39005 Santander, Spain.

*Corresponding author: glezpablo@unican.es

ciceros@unican.es

borja.arroyo@unican.es

jose.alvarez@unican.es

ARTICLE INFO

Keywords:

Hydrogen Embrittlement

Theory of Critical Distances

Environmentally-Assisted Cracking

Notch Effect

Cathodic Polarization

ABSTRACT

This paper provides a methodology, based on the Theory of Critical Distances (TCD), for the hydrogen embrittlement analysis of steels in cracked and notched conditions. The TCD has been successfully employed in fracture and fatigue analysis, but it has not yet been applied under environmentally assisted cracking conditions. The point method and the line method, both belonging to the TCD, have been applied to two steels (X80 and S420) following an experimental programme composed of C(T) specimens containing defects with notch radii varying from 0 mm up to 2 mm. Fracture mechanics tests were carried out at $6 \cdot 10^{-8}$ m/s of constant displacement rate under cathodic polarization conditions (5 mA/cm^2). The aqueous environment has been prepared following the Pressouyre's method. The study, which has been completed with finite element simulation analysis, reveals that the TCD provides accurate predictions of the hydrogen embrittlement behaviour of these steels in notched conditions.

1. Introduction

Predictions of the U.S. Department of Energy estimate that fossil fuels (petroleum, gas, and other liquid fuels) will remain the main source of energy until 2040. At the same time, nuclear power and renewables are growing in order to satisfy the energy demand, which is expected to present an increase of 48% by 2040 [1]. The increasing energy demand has led to the development of new infrastructures, many of which are located in offshore areas, operating in increasingly aggressive environments and poor conditions. The environment in which the resulting structural components operate can cause stress corrosion cracking (SCC) or hydrogen embrittlement (HE) phenomena, both of which may lead to brittle failure due to the degradation of the mechanical properties of the materials [2,3].

Nomenclature

Principal symbols

a	crack size
B	specimen thickness
E	Young's modulus
L	material critical distance
r	distance from the notch tip
W	specimen width
ρ	notch radius
B_N	net specimen thickness
e_u	ultimate strain
K_{mat}	fracture toughness
K_{mat}^N	apparent fracture toughness
K_{IEAC}	crack propagation threshold for EAC
K_{IEAC}^N	apparent crack propagation threshold for EAC
L_{EAC}	material critical distance for EAC
L_{EAC-BF}	best fit of material critical distance for EAC
P_Q	applied load when the crack starts propagation
ΔK_{th}	fatigue crack propagation threshold
$\Delta\sigma_0$	fatigue limit
σ_u	ultimate tensile strength
σ_Y	yield stress
σ_0	inherent strength
σ_{0EAC}	inherent strength for EAC

Principal abbreviations

EAC	Environmentally Assisted Cracking
FE	Finite Element
HE	Hydrogen Embrittlement
LEFM	Linear Elastic Fracture Mechanics
LM	Line Method
PM	Point Method
SCC	Stress Corrosion Cracking
TCD	Theory of Critical Distances

Nowadays, the behaviour of steels under Stress Corrosion Cracking (SCC) or Hydrogen Embrittlement (HE) conditions is a matter of great importance [4,5]. Repairs and replacements of components containing defects in offshore areas or power plants have become a highly affair. During fracture assessments, a common practice is to assume crack-like defects. However, defects may present a finite radius at their tip, and, in these cases, they are referred to as notches (e.g. corrosion defects, mechanical damage and fabrication defects). Assuming crack-like behaviour leads to overconservative results when defects are notches, given that notched components present an apparent fracture toughness which is greater than the fracture toughness observed in cracked components [6–9]. Hence, methodologies considering the real behaviour of notches are necessary.

Failure of components that present defects, such as cracks or notches, is a matter of great interest at present and can be assessed by two different criteria: the global criterion and local criteria. The latter criteria are more easily applicable due to the fact that they are based on the stress-strain field at the defect tip. Local approaches for the failure assessment of brittle and quasi-brittle materials such as Neuber's fictitious notch rounding approach, the notch stress intensity factor criterion, the generalized maximum tangential stress criterion and Sih's criterion involve averaging the stresses [10–13]. Other methodologies, such as the strain energy density or the equivalent material concept, can be linked to these approaches for predictions of brittle failure and in the presence of considerable plastic deformations [14–17].

In the last few decades, the most important group of methodologies capable of predicting the fracture behaviour of notched components has been developed under the name of Theory of Critical Distances (TCD). All these TCD methodologies employ a characteristic material length parameter, the critical distance (L), when performing fracture and fatigue assessments. The most relevant are the Point Method (PM) and the Line Method (LM), since they are the most simple and have been successfully applied in fracture and fatigue analyses [18–21].

The accuracy of the TCD in carrying out fracture and fatigue assessments in materials has been proved by numerous researchers. However, the TCD has not yet been employed in Environmentally Assisted Cracking (EAC) analyses. Hence, the aim of this study is to present, through a set of mechanical tests and finite element simulations, an analysis of EAC (Hydrogen Embrittlement in this case) based on the TCD. Two steels (X80 and S420), which are commonly used in power plants, offshore structures and pipes, have been employed in this work. Cathodic polarization (or cathodic charge) has been employed because of its wide use in industry to protect (against corrosion) components that operate in aggressive environments, causing steel embrittlement by the hydrogen action going through and getting trapped in the steel.

2. Theoretical background

2.1. The Theory of Critical Distances

The TCD is a group of methodologies all of which use a characteristic material length parameter, the critical distance (L) when performing fracture and fatigue assessments. The pioneering study was carried out both by Neuber in Germany [12,22] and Peterson in the United States [23,24]. Both researchers investigated fatigue failure in components containing notches. The work of these authors was applied to the prediction of brittle fracture in the 1960s by McClintock, Irwin and Novozhilov [25,26]. Whitney and Nuismer linked this theory to the theory of Linear Elastic Fracture Mechanics (LEFM) providing a theoretical relationship between the critical distance, L , and the fracture toughness in order to predict brittle failure in notched components [27]. In 1983, Tanaka presented the equation for fatigue analysis [28] which was later validated by Lazzarin, Taylor and Wang [29–32].

Nowadays, this theory is currently being developed providing accurate solutions to different engineering problems in a wide range of materials (e.g., metals, ceramics, polymers, composites, rocks, bones etc.) [21,33–41].

In fracture analysis, the above-mentioned critical distance, L , follows this equation [18]:

$$L = \frac{1}{\pi} \left(\frac{K_{mat}}{\sigma_0} \right)^2 \quad (1)$$

where K_{mat} is the material fracture toughness (derived from cracked specimens) and σ_0 is a characteristic strength parameter, known as the inherent strength. In steels, the inherent strength is usually larger than the ultimate tensile strength, σ_u , and requires calibration.

Analogously, in fatigue analysis, $\Delta\sigma_0$ is the plain specimen fatigue strength, ΔK_{th} is the fatigue crack propagation threshold, with L following equation (2) [18,19]:

$$L = \frac{1}{\pi} \left(\frac{\Delta K_{th}}{\Delta\sigma_0} \right)^2 \quad (2)$$

When using the TCD through any of its two simplest methodologies, which are the Point Method (PM) and the Line Method (LM), predictions in fracture and fatigue analyses can be made when the stress-strain field around the stress concentration feature is known [18].

2.1.1. The Point Method (PM)

The simplest form of the TCD is the PM. This method establishes that fracture occurs when the stress at a distance of $L/2$ from the notch tip is equal to the inherent strength, σ_0 . The mathematical equation is [18]:

$$\sigma \left(\frac{L}{2} \right) = \sigma_0 \quad (3)$$

An analogous approach can be used in order to predict failure in fatigue [18]:

$$\Delta\sigma \left(\frac{L}{2} \right) = \Delta\sigma_0 \quad (4)$$

Stress-distance curves at the notch tip in fracture (a) and fatigue (b) are shown in Fig. 1. TCD parameters (the critical distance, L , and the inherent strength, σ_0) can be obtained by performing only two fracture (or fatigue) tests on two samples which present different defects (e.g., different notch radii), as shown in Fig. 1a)

(a)

(b)

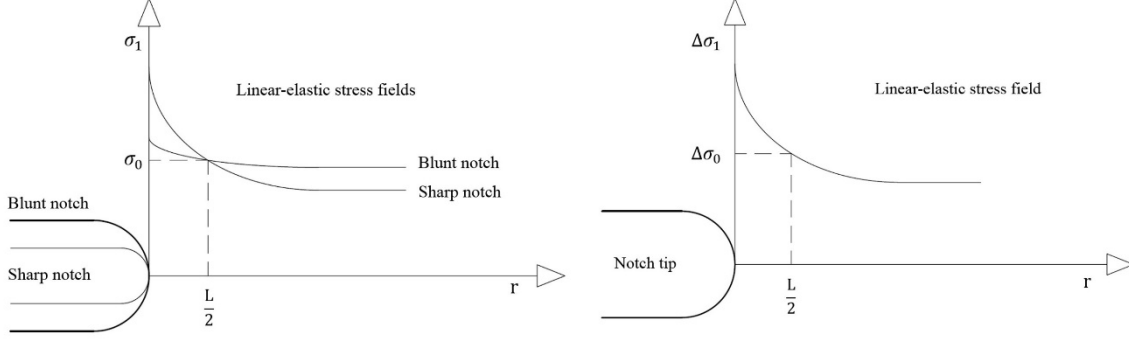


Fig. 1. Obtaining TCD parameters through the stress-distances curves at the notch tip in (a) fracture and (b) fatigue analyses.

The stress-distance curves cross each other at one point with coordinates $(L/2, \sigma_0)$ in fracture assessments or $(L/2, \Delta\sigma_0)$ in fatigue analysis.

Equations predicting the apparent fracture toughness (exhibited by U-notched components), K_{mat}^N , may be provided by the PM. To do so, it is necessary to consider the linear-elastic stress field at the defect tip, provided by Creager-Paris (equation (5)) [42]:

$$\sigma(r) = \frac{K}{\sqrt{\pi}} \frac{2(r + \rho)}{(2r + \rho)^{3/2}} \quad (5)$$

where K is the stress intensity factor defined for a crack with the same length as the notch, r is the distance from the notch tip and ρ is the notch radius. Equation (5) was obtained for long thin U-shaped notches and is only valid for small distances from the notch tip ($r \ll$ notch depth). Assuming that failure occurs when K_I is equal to K_{mat}^N and combining equations (3) and (5), a new expression is obtained (equation (6)) [18]:

$$K_{mat}^N = K_{mat} \frac{\left(1 + \frac{\rho}{L}\right)^{3/2}}{\left(1 + \frac{2\rho}{L}\right)} \quad (6)$$

This expression provides predictions of the apparent fracture toughness exhibited by U-notched components.

2.1.2. The Line Method (LM)

The LM considers the average stress over some distance from the notch tip, starting at $r=0$. This distance is equal to $2L$, L being obtained from equation (1). Thus, the LM criterion for fracture assessments can be defined, employing the same definition of L as above, by equation (7) [18]:

$$\frac{1}{2L} \int_0^{2L} \sigma(r) dr = \sigma_0 \quad (7)$$

Analogously, the LM criterion for fatigue analysis is defined by the following expression [18]:

$$\frac{1}{2L} \int_0^{2L} \Delta\sigma(r) dr = \Delta\sigma_0 \quad (8)$$

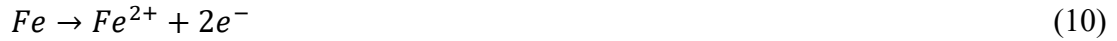
Following analogous assumptions as those considered for the PM, predictions of the apparent fracture toughness, K_{mat}^N , can be made combining equations (5) and (7). The result is a simple expression [18]:

$$K_{mat}^N = K_{mat} \sqrt{1 + \frac{\rho}{4L}} \quad (9)$$

2.2. Hydrogen embrittlement

Most steels containing hydrogen present premature failures when they are stressed in tension. This kind of hydrogen damage, known as hydrogen embrittlement (HE), reduces ductility and is the basic mechanism that controls the EAC.

Hydrogen can cause embrittlement in metals by the action of atoms penetrating into the microstructure and diffusing to the plastic areas (most stressed zones) [5]. In order for HE failure to occur, a susceptible material, an exposure to hydrogen-containing environment and a high enough stress are required. The above-mentioned exposure to an aggressive environment involves a corrosion process whose anodic reaction is:



The oxygen is reduced at the metal surface, the cathodic reaction being:



In acidic solutions (i.e., pH<4), meanwhile, the cathodic hydrogen evolution is [5]:



One of the most widely used methods of corrosion prevention is cathodic protection (or cathodic charge) because it reduces the corrosion rate if a potential (or current density) below the open circuit potential is applied by means of a cathodic polarization between the anode and the cathode, usually provided by an external source. The main disadvantage is that it also increases the H₂ production [5]. If the polarization of the system is excessive, a direct reduction of H₂O is possible, as shown below:



In these cases, hydrogen causes the breakage of protective layers and damages the material below by HE [43]. Before the H₂ molecule formation, H atoms are present on the metal surface during a significant time, which is increased by the presence of cathodic

poisons (e.g., S^{2-} and As^{3+}). Hydrogen atoms can penetrate into interstitial sites facilitated by its small size causing embrittlement [44].

3. Materials and methods

3.1. Materials

Two steels were employed in this study. Firstly, a rolled X80 medium-strength steel [45], which is used in petroleum and gas transportation at low temperatures. Secondly, a weldable thermo-mechanically treated S420 medium-strength steel [46], which is mainly employed in offshore structures, power plants and pressure vessels. The chemical composition of these steels is shown in Table 1.

Table 1 Chemical composition of the two steels analysed (weight %).

	C	Si	S	P	Mn	Ni	Cr	Mo	Cu	Al	V	Ti	Nb
X80	0.07	0.18	<0.005	<0.005	1.83	0.03	-	0.15	0.02	0.03	-	-	0.03
S420	0.08	0.28	0.001	0.012	1.44	0.03	0.02	0.003	0.015	0.036	0.005	0.015	0.031

The microstructure of the steels analysed in this work is shown in Fig. 2. Both X80 and S420 steels present a ferritic-pearlitic microstructure with a grain size ranging between 5-15 μm and 5-25 μm respectively. The mechanical properties of these steels, as received and exposed to the aggressive environment, are gathered in Table 2.

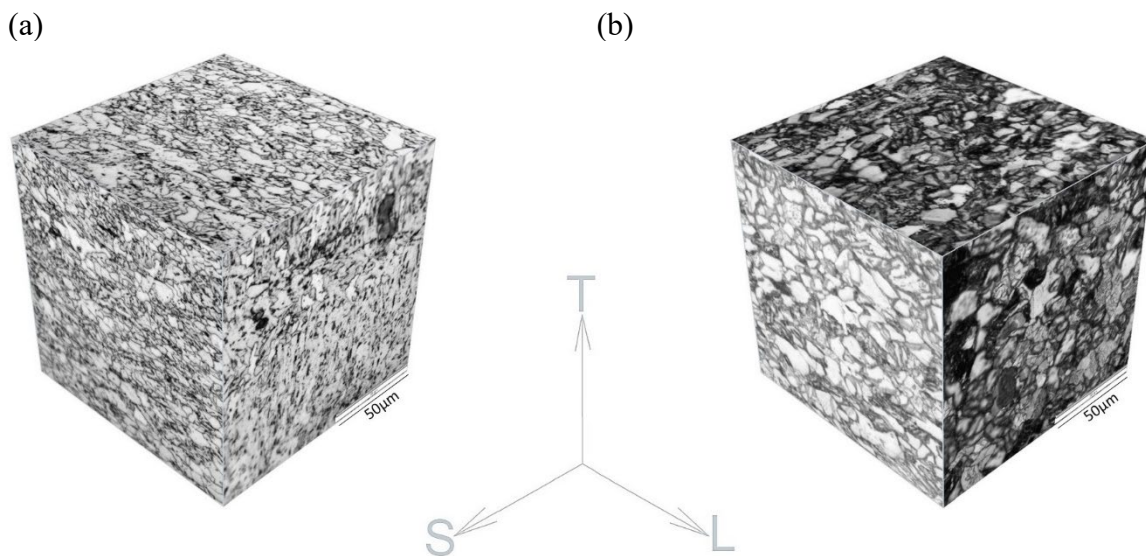


Fig. 2. Microstructure of (a) X80 and (b) S420 steels.

Table 2. Mechanical properties of the two steels analysed, as received and exposed to the aggressive environment.

Material	E (GPa)	Air	Aggressive environment
----------	---------	-----	------------------------

	σ_y (MPa)	σ_u (MPa)	e_u (%)	σ_y (MPa)	σ_u (MPa)	e_u (%)	
X80	209.9	621.3	692.9	29.6	492.6	492.6	0.34
S420	206.4	447.7	547.1	21.7	348.6	348.6	0.20

Tensile stress-strain curves of the materials in air and subjected to the aggressive environment are shown in Fig. 3.

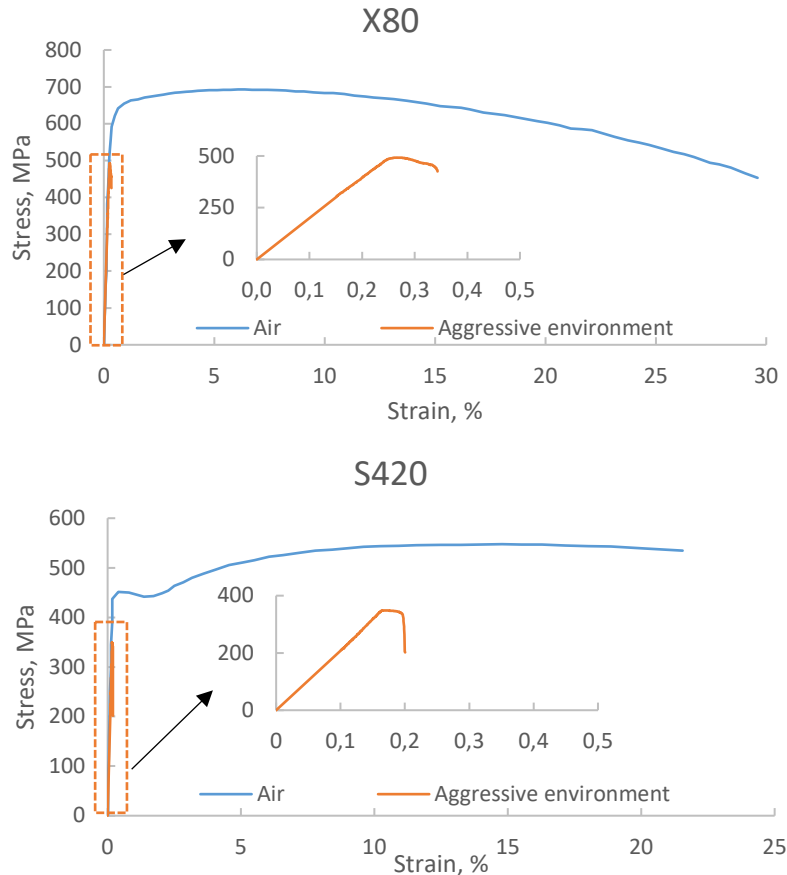


Fig. 3. Tensile Stress-Strain curves of X80 and S420 steels in air and exposed to the aggressive environment.

3.2. Simulation of cathodic polarization and hydrogen embrittlement

In this study, cathodic polarization will be used to cause embrittlement on the metal, imposing a fixed current intensity [43]. The steel and the noble metal (platinum in this case) are connected through an aqueous solution at $5\text{mA}/\text{cm}^2$ due to its common use in gas and oil pipes and offshore structures in order to reproduce local HE phenomena. The aqueous solution used in this study has been an acidic electrolyte, prepared following the Pressouyre's method [47]. It consists of an 1N H_2SO_4 solution in distilled water with 10mg of an As_2O_3 solution and 10 drops of CS_2 per liter of dissolution. During the test, the pH is kept in the range 0.65-0.80 at room temperature. Out of this pH range, the solution has to be changed [47-49].

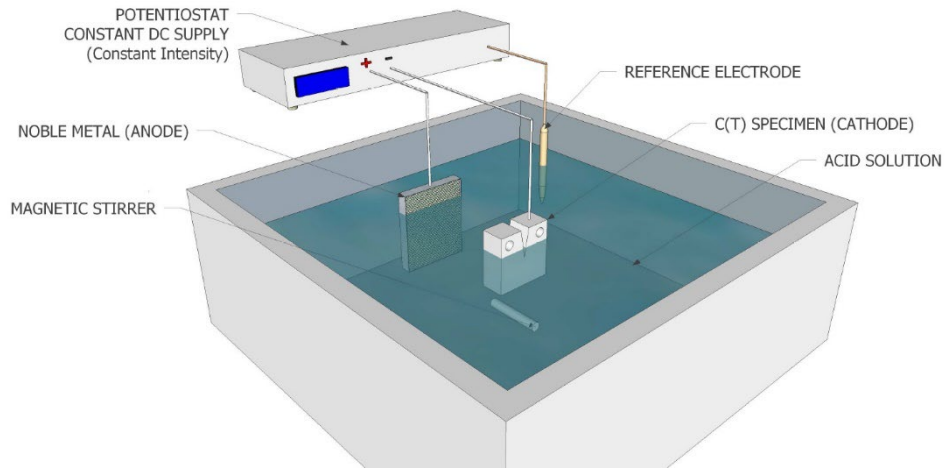


Fig. 4. Schematic of the cathodic polarization used in this work.

The aqueous solution is stirred to remove hydrogen bubbles on the specimen surface and prevent localized corrosion (e.g., pits). A schematic of the cathodic polarization and the test carried out, respectively, are shown in Fig. 4 and Fig. 5. In the test, the C(T) specimen, a platinum grid and the saturated calomel electrode are used as the working electrode, the counter electrode and the reference electrode, respectively.



Fig. 5. Set up of the test under cathodic polarization.

3.3. A methodology for analysing EAC using the TCD

The TCD provides failure predictions in fracture and fatigue analyses. In this work, the TCD is reformulated to address the EAC problem. In order to obtain the characteristic length parameter in EAC and following equations (1) and (2), an analogous expression has been proposed:

$$L_{EAC} = \frac{1}{\pi} \left(\frac{K_{IEAC}}{\sigma_{0EAC}} \right)^2 \quad (14)$$

where L_{EAC} is the EAC critical distance, K_{IEAC} is the EAC crack propagation threshold (calculated from cracked specimens) and σ_{0EAC} is the inherent strength under EAC conditions which has to be calibrated [50].

Assuming this expression for the EAC critical distance determination, crack initiation predictions in U-shaped notches caused by EAC can be made by comparing the applied stress intensity factor with the apparent EAC crack propagation threshold (K_{IEAC}^N). In this case, the PM generates equation (15):

$$K_{IEAC}^N = K_{IEAC} \frac{\left(1 + \frac{\rho}{L_{EAC}}\right)^{3/2}}{\left(1 + \frac{2\rho}{L_{EAC}}\right)} \quad (15)$$

and the LM provides equation (16):

$$K_{IEAC}^N = K_{IEAC} \sqrt{1 + \frac{\rho}{4L_{EAC}}} \quad (16)$$

Both methods allow the apparent EAC crack propagation threshold, K_{IEAC}^N , of a material containing a U-shaped notch, to be calculated from the notch radius, ρ , the material EAC critical distance, L_{EAC} , and the material EAC crack propagation threshold, K_{IEAC} (calculated in cracked conditions following well-known standards (e.g. [51])).

3.4. Experimental programme

In the EAC context, mechanical variables such as loading type and loading rate affect the crack propagation threshold (K_{IEAC}) and the crack propagation rate [52]. In this work, fatigue pre-cracked C(T) specimens and notched C(T) specimens, as shown in Fig. 6, have been tested under the constant displacement method using a slow strain rate machine [51]. A displacement rate of $6 \cdot 10^{-8}$ mm/s has been used in each material. In all cases specimens were obtained in T-L orientation.

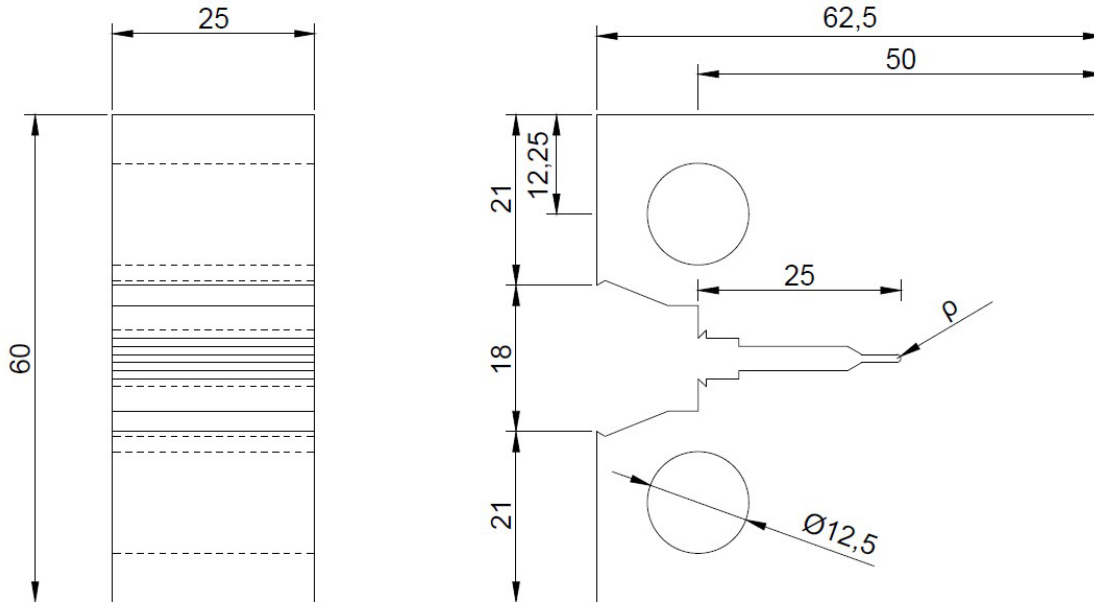


Fig. 6. Geometry of the tested specimens (dimensions in mm).

Table 3 gathers a summary of the experimental programme, which is composed of 20 C(T) specimens with radii varying from 0 mm (crack-like defect) up to 2 mm. As shown in Fig. 6, a standard geometry of C(T) specimens has been used [51]. In order to obtain more accuracy, the tests have been duplicated for each notch radius.

Before testing, both cracked and notched specimens were exposed to hydrogen absorption for 48 hours, being submerged in the cathodic polarization environment to a sufficient degree as to ensure that the defect tip will always be covered [53]. After the hydrogen absorption due to cathodic polarization, mechanical testing started using a slow strain rate machine. During the tests, the specimens were subjected to constantly rising displacement while being exposed to the cathodic charge [54,55]. In this case, the constant displacement rate is $6 \cdot 10^{-8}$ mm/s. Load-COD curves were obtained for each test.

In spite of the relatively low applied displacement rate, an important advantage is the rapidity with which EAC susceptibility can be assessed in comparison with other methodologies (e.g., constant load test, double cantilever beam, C-ring) [55].

Table 3 Summary of the experimental programme.

Material	Displacement rate (m/s)	ρ (mm)	Number of tests
X80	$6 \cdot 10^{-8}$	0.00	2
		0.25	2
		0.50	2
		1.00	2
		2.00	2
S420	$6 \cdot 10^{-8}$	0.00	2
		0.25	2

0.50	2
1.00	2
2.00	2

The methodology proposed by ISO 7539 [51] was employed in order to calculate K_{IEAC} . The governing expression of these methodologies is:

$$K_{IEAC} = \frac{P_Q}{(BB_N W)^{1/2}} f\left(\frac{a}{W}\right) \quad (17)$$

For C(T) specimens the expression of the geometrical factor, $f(a/W)$, follows equation (18):

$$f\left(\frac{a}{W}\right) = \frac{\left[\left(2 + \frac{a}{W}\right) \left(0.886 + 4.64 \frac{a}{W} - 13.32 \left(\frac{a}{W}\right)^2 + 14.72 \left(\frac{a}{W}\right)^3 - 5.6 \left(\frac{a}{W}\right)^4 \right) \right]}{\left(1 - \frac{a}{W}\right)^{3/2}} \quad (18)$$

P_Q is the applied load when the crack starts to propagate due to EAC, B is the specimen thickness, B_N is the net specimen thickness ($B = B_N$ if no side grooves are present), W is the specimen width and $f(a/W)$ is a geometrical factor depending on the crack size, a , and the specimen width, W . These equations were applied to both cracked specimens (generating K_{IEAC} values) and notched specimens (generating K_{IEAC}^N values).

3.5. Finite Element Analysis

A FE modelling of the C(T) specimen was built in Abaqus. The analysis was performed in order to determine the stress field at the notch tip when the crack starts to propagate. According to the literature [18], the simulation was carried out in linear elastic conditions. The mesh, which has been created employing hexahedric elements, is much more refined close to the notch tip because of the higher gradients in this zone.

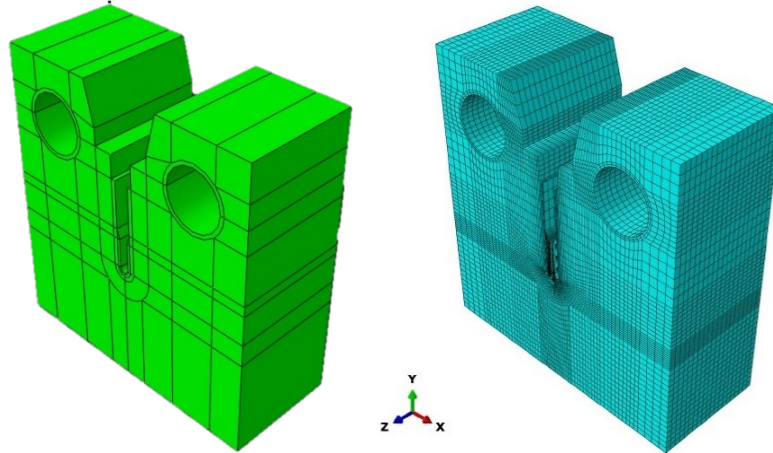


Fig. 7. FE model employed to simulate the tests.

The structured meshing technique has been employed and the model has been developed using C3D8R 3D solid elements with a reduced integration. This 3D model requires manual

partitioning, which has been performed following the specimen shape in order to mesh the most complex regions such as the notch tip and the holes. Each partition has been carried out according to the geometry of the specimen and the mesh has been created by number of elements rather than by element size so that the notch tip presents 60 elements around the perimeter and 30 elements along the width. As the distance moves away from the notch tip the mesh becomes thicker. Fig. 7 represents the FE model employed together with the mesh.

4. Results and discussion

The results of P_Q and the corresponding apparent EAC crack propagation threshold, K_{IEAC}^N , are gathered in Table 4. The values of K_{IEAC}^N have been obtained following the methodology proposed in ISO 7539 and using equations (17) and (18). For cracked specimens, K_{IEAC}^N coincides with K_{IEAC} .

Table 4. Experimental results of K_{ISCC}^N .

Material	Specimen	ρ (mm)	P_Q (kN)	K_{IEAC}^N (MPa·m ^{0.5})
X80	X80-1	0.00	27.86	67.42
	X80-2	0.00	23.12	53.16
	X80-3	0.25	34.41	63.21
	X80-4	0.25	34.85	64.01
	X80-5	0.50	38.26	70.28
	X80-6	0.50	42.75	78.52
	X80-7	1.00	44.50	81.74
	X80-8	1.00	42.93	78.87
	X80-9	2.00	48.59	89.25
	X80-10	2.00	54.20	99.56
S420	S420-1	0.00	28.76	67.58
	S420-2	0.00	24.01	61.25
	S420-3	0.25	34.70	63.74
	S420-4	0.25	33.94	62.34
	S420-5	0.50	37.09	68.13
	S420-6	0.50	34.21	62.84
	S420-7	1.00	41.09	75.48
	S420-8	1.00	40.49	74.37
	S420-9	2.00	45.45	83.49
	S420-10	2.00	45.67	83.89

The K_{IEAC} values used here to apply the TCD have been obtained as the average value of K_{IEAC} in precracked specimens ($\rho = 0$ mm). Thus, the experimental values of EAC crack propagation threshold in X80 and S420 steels are, respectively, 60.29 MPa·m^{0.5} and 64.42 MP·m^{0.5} (as shown in Table 6).

Table 5 shows that the S420 steel does not fulfil the recommendation for size independency. However, following the standard ISO 7539 [51], the presence of an aggressive environment during the test reduces the extent of plasticity associated with fracture and hence the sample dimensions needed in order to limit plastic deformation. Thus, a minimum

thickness cannot be specified. In any case, regardless of whether or not K_{IEAC} is size independent for the specimens being tested, the analysis performed allows the results obtained for the different notch radii to be compared.

Table 5. Recommended specimen thickness following ISO 7539

	K_{IEAC} (MPa·m ^{0.5})	σ_y (MPa)	Min. recommended thickness (mm)
X80	60.29	621.3	23.5
S420	64.42	447.7	51.7

In order to obtain the TCD parameters (L_{EAC} and σ_{0EAC}), FE simulations were carried out in linear elastic conditions and applying P_Q , which is the load at crack propagation onset (gathered in Table 4). The TDC assumes linear-elastic conditions although the real situation may have nonlinearities. This may be done and has been widely validated once σ_0 is calibrated. In other words, under non-linear conditions, σ_0 becomes a parameter that converts a non-linear situation into an equivalent linear-elastic one. [18,56].

Stress fields at the notch tip and stress-distance curves in the central line of the middle section were obtained, as shown in Fig. 8 and Fig. 9 respectively.

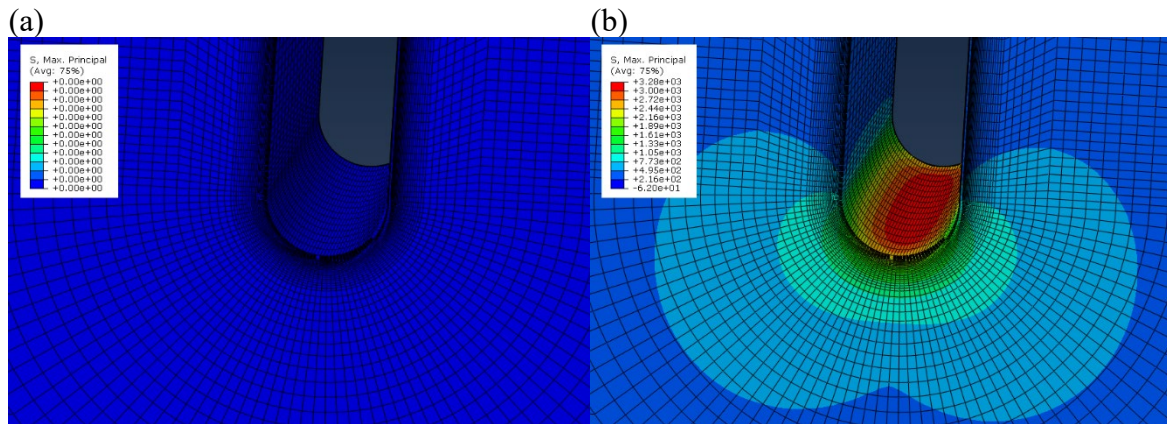


Fig. 8. Principal stress distribution around the notch tip in C(T) notched specimen (a) before the test and (b) after the simulation (X80 steel and $\rho=1.00$ mm).

It can be observed that the different curves cross each other at approximately one point, with coordinates $(L_{EAC}/2, \sigma_{0EAC})$, as this work postulates following the assumption of the PM. The value of the experimental L_{EAC} has been obtained as the average value at the different crossing points. In the case of X80 steel, $L_{EAC} = 0.286$ mm ($L_{EAC}/2 = 0.143$ mm) and $\sigma_{0EAC} = 2630$ MPa (Fig. 9-a), while for S420 steel, $L_{EAC} = 0.462$ mm ($L_{EAC}/2 = 0.231$ mm) and $\sigma_{0EAC} = 2101$ MPa (Fig. 9-b).

As noted previously, the analysis has been performed in linear elastic conditions because the critical distance in EAC (L_{EAC}) method described in this paper requires only linear-elastic stress analysis [18]. As a result of ignoring the yielding of the material, the values of the inherent strength for EAC (σ_{0EAC}) have been large.

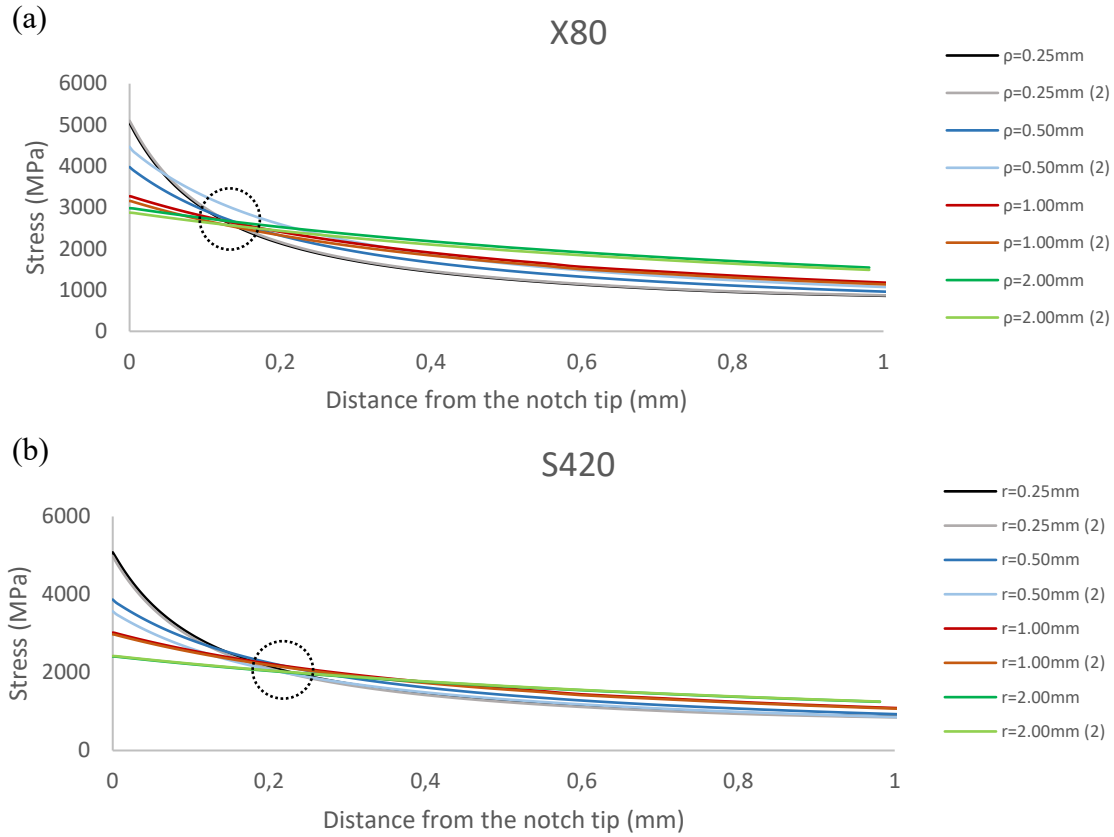


Fig. 9. Stress-distance curves at crack initiation in (a) X80 and (b) S420 C(T) notched specimens.

Once K_{IEAC} and L_{EAC} have been calculated, predictions of K_{IEAC}^N can be easily derived for each notch radius following the PM, equation (15), or the LM, equation (16). The accuracy of these methodologies is determined by comparing the experimental results with the predictions of K_{IEAC}^N .

Table 6 gathers the experimental values of L_{EAC} and the value of the EAC critical distance providing the best fit of the experimental results depending on the methodology. The latter parameter has been calculated by performing the best fit (least squares) of the PM and LM predictions (equations (15) and (16), respectively) of K_{IEAC}^N with L_{EAC} being the fitting parameter.

Table 6. Values of K_{IEAC} , EAC critical distance and the best fit depending on the methodology.

Material	Displacement rate (m/s)	K_{IEAC} (MPa·m ^{0.5})	L_{EAC} (mm)	PM L_{EAC} -BF (mm)	LM L_{EAC} -BF (mm)
X80	$6 \cdot 10^{-8}$	60.29	0.286	0.197	0.276
S420		64.42	0.461	0.386	0.776

The experimental results of K_{IEAC}^N and predictions provided by PM and LM (equations (15) and (16) respectively) using the experimental EAC critical distance (L_{EAC}) and the best

fit of the experimental EAC critical distance (L_{EAC-BF}) for X80 and S420 steels are shown in Fig. 10 and Fig. 11.

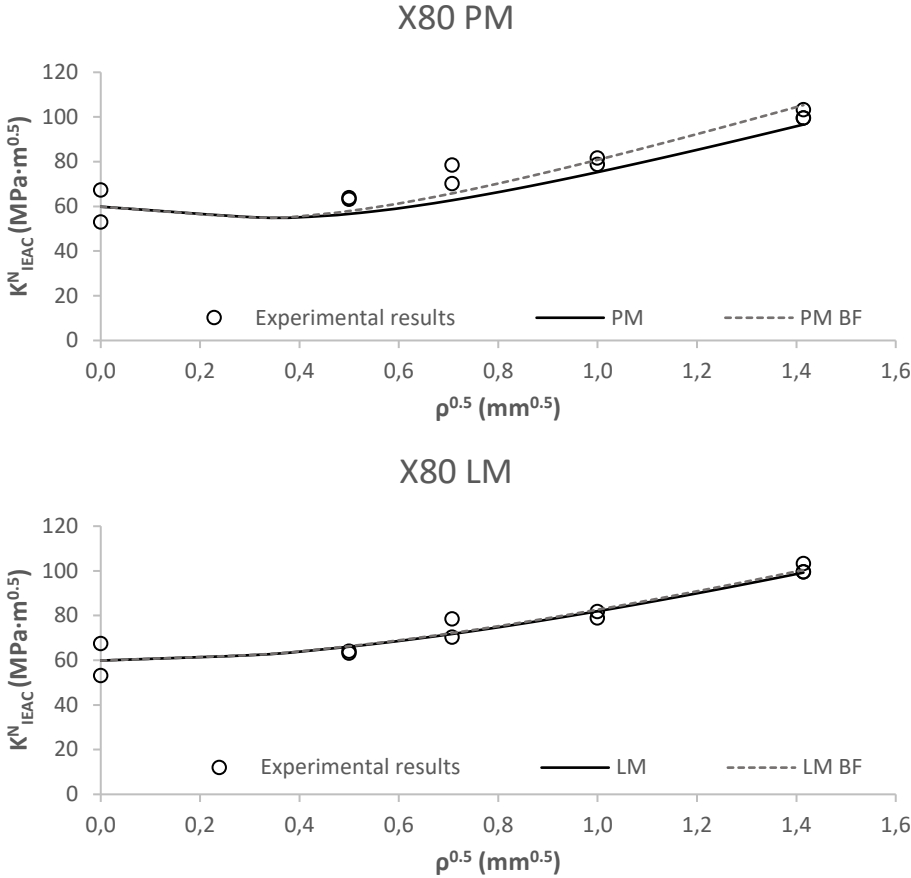


Fig. 10. PM and LM predictions in X80 steel.

Both PM and LM provide suitable predictions of K^N_{IEAC} . An evident notch effect with an increase of K^N_{IEAC} with the notch radius, ρ , has been observed. This notch effect is especially significant in X80 steel.

The experimental results show that there is a notch radius, 0.25 mm in X80 steel and 0.25-0.50 mm in S420 steel, below which K^N_{IEAC} remains basically constant. The PM, which is capable of predicting this behaviour, provides K^N_{IEAC} predictions which are more conservative than those obtained with the LM. This conservative trend may also be related with the fact that the calibration of L_{EAC} has been performed using the PM definition. In case of the LM, predictions tend to overestimate K^N_{IEAC} in S420 steel.

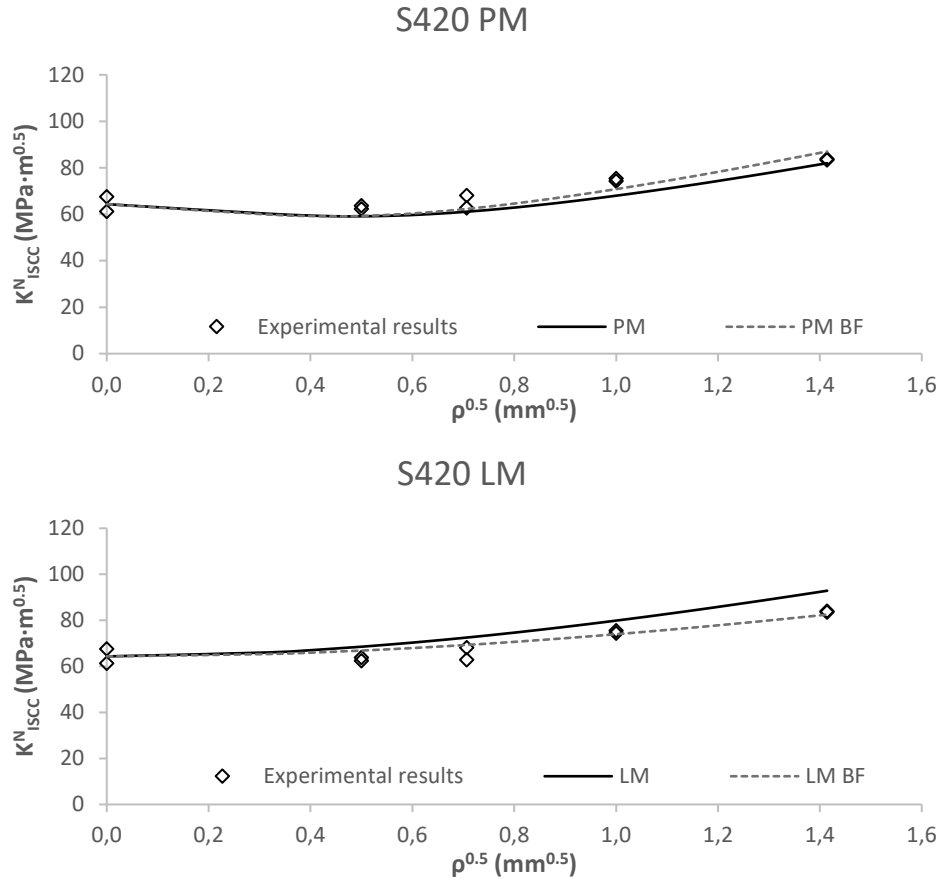


Fig. 11. PM and LM predictions in S420 steel.

4.1. SEM Analysis

Once the tests were completed, the two parts of each C(T) specimen were submitted to an ultrasonic cleaning with acetone for 30 min. Then, fracture surfaces were studied with a scanning electron microscope (SEM) in order to analyse fracture mechanisms.

Macro-images and fracture surfaces of X80 and S420 steels, varying the notch radius, are shown, respectively, in Fig. 12 and Fig. 13. Similar fracture mechanisms have been observed for the different notch radii. In other words, the notch effect does not apparently affect the fracture initiation mechanism, something which is in contradiction with the observations made in the analysis of ordinary fracture processes (e.g., [38,57–60]).

Fig. 12-a and Fig. 13-a show the fracture surfaces of precracked specimens in X80 and S420 steels respectively. Two different zones have been observed, fatigue precracking zone and crack propagation due to EAC.

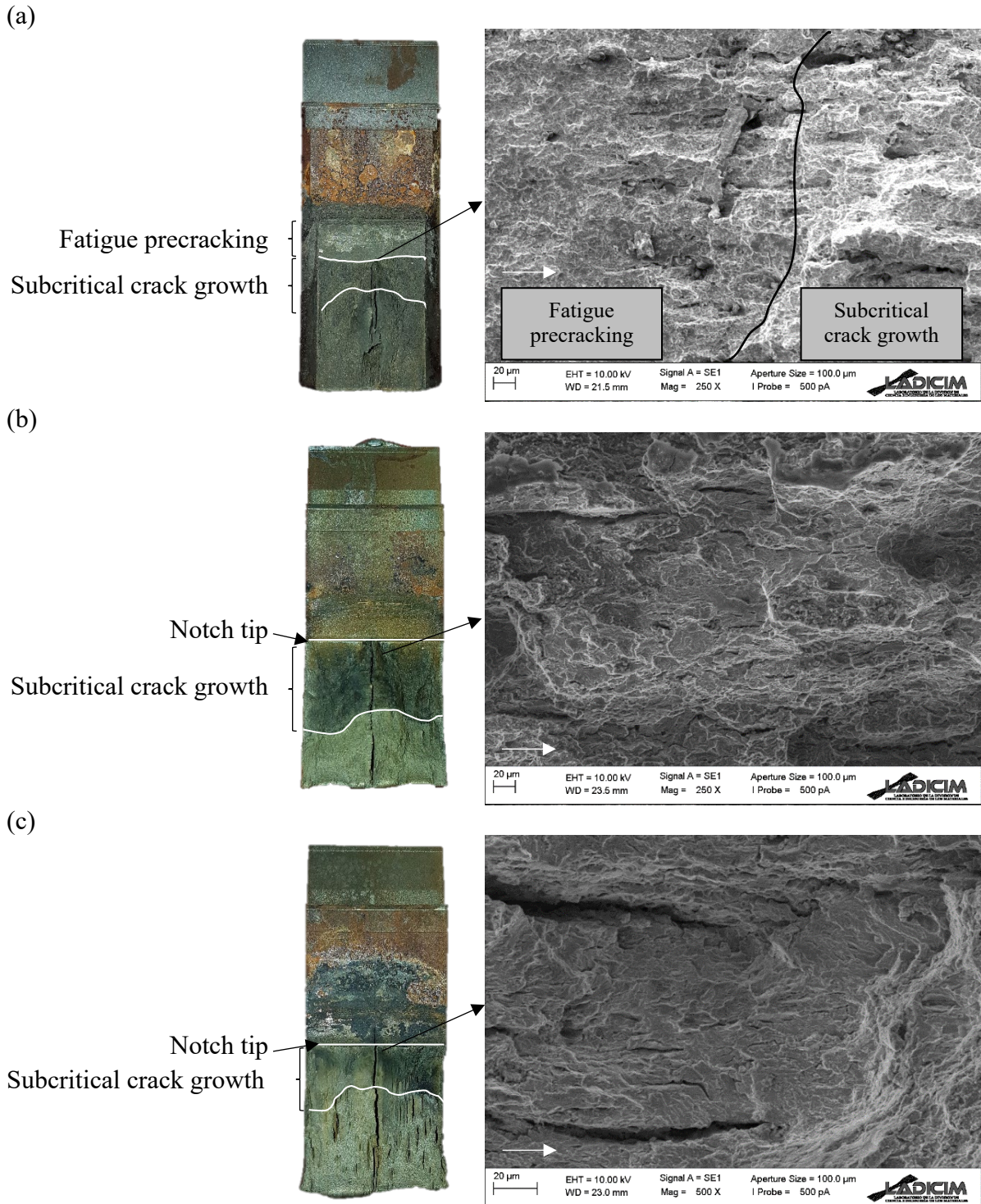


Fig. 12. Macro-images and fracture surfaces observed in X80 steel. (a) $\rho = 0.00$ mm; (b) $\rho = 0.50$ mm; (c) $\rho = 2.00$ mm.

X80 steel suffers a delamination process that comes from the formation of unconnected layers during the manufacturing process [61]. This can be appreciated in the macro-images of the analysed samples, where a discontinuity is present in the middle of the thickness parallel to the plane LT (Fig. 12).

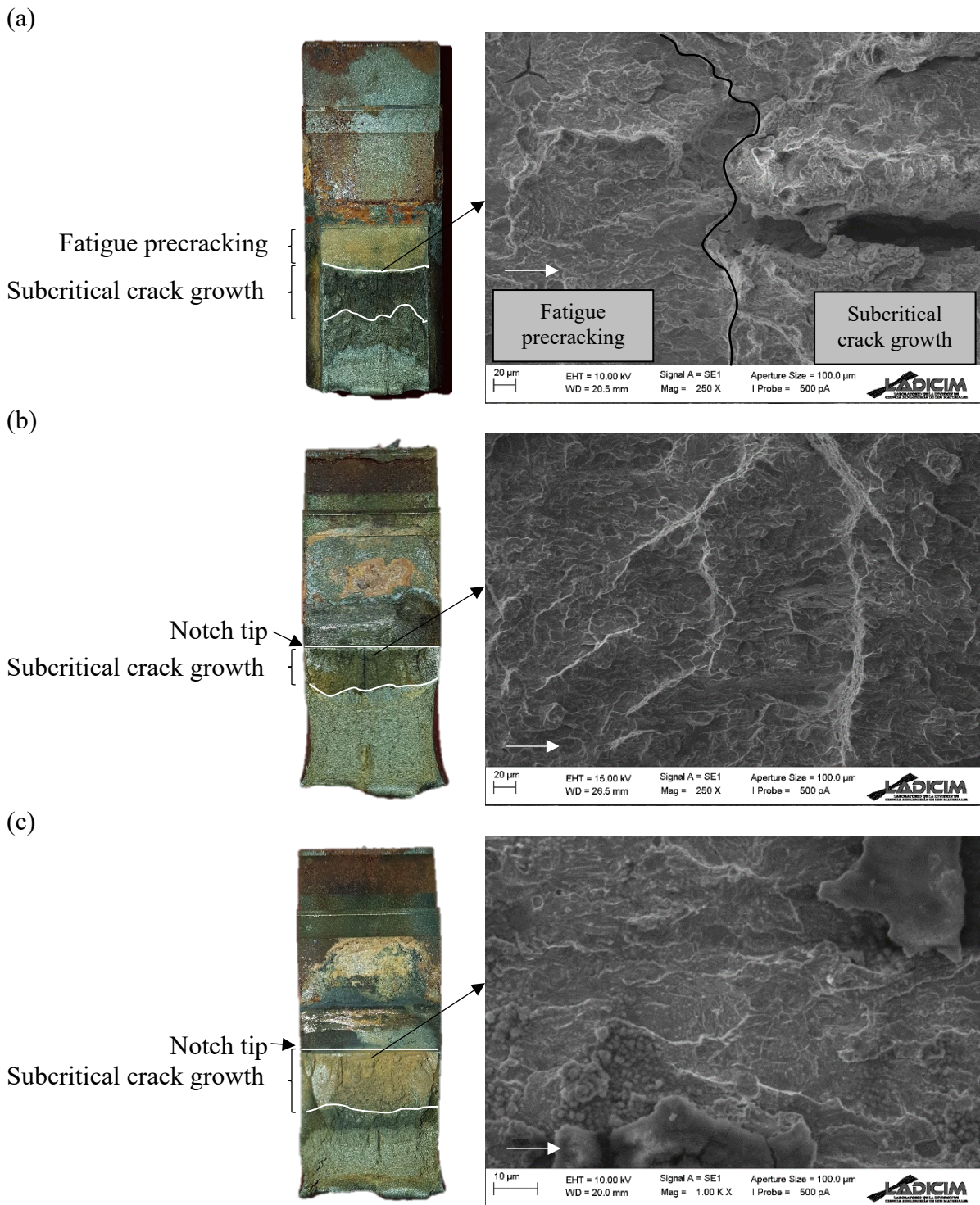


Fig. 13. Macro-images and fracture surfaces observed in S420 steel. (a) $\rho = 0.00$ mm; (b) $\rho = 0.50$ mm; (c) $\rho = 2.00$ mm

Based on the fracture surface appearance, cleavage and quasi-cleavage fracture, which involve subcritical crack propagation, were observed in both X80 and S420 steels (Fig. 12

and Fig. 13). These fracture mechanisms are a common feature caused by hydrogen induced fracture surfaces [62].

5. Conclusions

In this paper, the Theory of Critical Distances has been reformulated to address the Environmentally Assisted Cracking issue in steels. The TCD has been applied through the Point Method and the Line Method to predict the apparent crack propagation threshold in notched components, K_{IEAC}^N , under hydrogen embrittlement conditions caused by cathodic polarization at a level of 5 mA/cm². Its application has been proved through tests using constant displacement rate ($6 \cdot 10^{-8}$ m/s). The experimental results have been calculated in terms of K_{IEAC}^N . TCD parameters have been obtained by a combination of experimental tests and finite element simulations.

Both materials have presented an evident notch effect, which is more significant in the X80 steel. The Point Method and the Line Method predict this tendency providing accurate results. The stress field at the crack propagation onset of the different specimens (and notch radii) demonstrates that the PM criterion is fulfilled in EAC conditions.

The inherent strength obtained in this EAC analysis, σ_{0EAC} , shows values which are much larger than the ultimate tensile strength. Thus, this parameter requires calibration.

Based on the fracture surface appearance obtained from SEM analysis, cleavage and quasi-cleavage fractures (causing subcritical crack growth) have been observed. These fracture mechanisms are common in fracture surfaces of specimens which have been tested under constant displacement in Hydrogen Embrittlement conditions.

6. Acknowledgements

This work was supported by the Spanish Ministry of Science and Innovation through the research projects MAT2014-58443-P and MAT2014-58738-C3-3-R developed by the University of Cantabria.

References

- [1] International energy outlook 2016. Washington: U.S. Energy Information Administration; 2016.
- [2] Gangloff RP. Hydrogen-assisted Cracking. Compr Struct Integr 2003;6:31–101. doi:10.1016/B0-08-043749-4/06134-6.
- [3] Brown BF. Stress corrosion cracking control measures. Natl Bur Stand Monogr 1977.
- [4] Koch G. Cost of corrosion. Trends Oil Gas Corros Res Technol 2017;3–30. doi:10.1016/B978-0-08-101105-8.00001-2.
- [5] Jones DA. Principles and prevention of corrosion. New Jersey: Prentice-Hall, Inc. Simon & Schuster; 1996.
- [6] Atzori B, Lazzarin P, Filippi S. Cracks and notches: Analogies and differences of the relevant stress distributions and practical consequences in fatigue limit predictions. Int J Fatigue 2001;23:355–62. doi:10.1016/S0142-1123(00)00107-9.
- [7] Nui LS, Chehimi C, Pluvinage G. Stress field near a large blunted tip V-notch and application of the concept of the critical notch stress intensity factor (NSIF) to the fracture toughness of very brittle materials. Eng Fract Mech 1994;49:325–35. doi:10.1016/0013-7944(94)90262-3.

- [8] Pluvillage G. Fatigue and fracture emanating from notch; the use of the notch stress intensity factor. *Nucl Eng Des* 1998;185:173–84. doi:10.1016/S0029-5493(98)00183-6.
- [9] Fenghui W. Prediction of intrinsic fracture toughness for brittle materials from the apparent toughness of notched-crack specimen. *J Mater Sci* 2000;35:2543–6. doi:10.1023/A:1004746508509.
- [10] Torabi AR, Ayatollahi MR. Compressive brittle fracture in V-Notches with end holes. *Eur J Mech A/Solids* 2014;45:32–40. doi:10.1016/j.euromechsol.2013.11.012.
- [11] Berto F, Lazzarin P, Radaj D. Fictitious notch rounding concept applied to V-notches with root hole subjected to in-plane mixed mode loading. *Eng Fract Mech* 2014;128:171–88. doi:10.1016/J.ENGFRACMECH.2014.07.014.
- [12] Neuber H. Theory of notch stresses: principles for exact calculation of strength with reference to structural form and material. vol. 4547. Berlin: Springer Verlag; 1958.
- [13] Berto F, Lazzarin P. Recent developments in brittle and quasi-brittle failure assessment of engineering materials by means of local approaches. *Mater Sci Eng R Reports* 2014;75:1–48. doi:10.1016/J.MSER.2013.11.001.
- [14] Torabi AR, Habibi R, Mohammad Hosseini B. On the Ability of the Equivalent Material Concept in Predicting Ductile Failure of U-Notches under Moderate- and Large-Scale Yielding Conditions. *Phys Mesomech* 2015;18:337–47. doi:10.1134/s1029959915040062.
- [15] Torabi AR, Campagnolo A, Berto F. Mixed mode I/II crack initiation from U-notches in Al 7075-T6 thin plates by large-scale yielding regime. *Theor Appl Fract Mech* 2016;86:284–91. doi:10.1016/j.tafmec.2016.08.002.
- [16] Torabi AR, Berto F. Fracture assessment of blunt V-notched graphite specimens by means of the strain energy density. *Strength Mater* 2013;45:635–47. doi:10.1007/s11223-013-9500-z.
- [17] Torabi AR, Berto F. Mixed mode fracture assessment of U-notched graphite Brazilian disk specimens by means of the local energy. *Struct Eng Mech* 2014;50:723–40. doi:10.12989/sem.2014.50.6.723.
- [18] Taylor D. The Theory of Critical Distances. 2007. doi:10.1016/B978-0-08-044478-9.X5000-5.
- [19] Susmel L. The theory of critical distances: a review of its applications in fatigue. *Eng Fract Mech* 2008;75:1706–24. doi:10.1016/J.ENGFRACMECH.2006.12.004.
- [20] Cicero S, Madrazo V, Carrascal I, García T. The use of the theory of critical distances in fracture and structural integrity assessments. *Res. Appl. Struct. Eng. Mech. Comput. - Proc. 5th Int. Conf. Struct. Eng. Mech. Comput. SEMC 2013, 2013*, p. 573–8.
- [21] Taylor D, Kasiri S, Brazel E. The theory of critical distances applied to problems in fracture and fatigue of bone. *Frat Ed Integrità Strutt* 2009;3. doi:10.3221/IGF-ESIS.10.02.
- [22] Neuber H. Theorie der technischen Formzahl. *Forsch Auf Dem Gebiete Des Ingenieurwesens* 1936;7:271–4. doi:10.1007/BF02584908.
- [23] Peterson RE. Notch sensitivity. *Met Fatigue* 1959:293–306.
- [24] Peterson RE. Methods of correlating data from fatigue tests of stress concentration specimens. *Stephen Timoshenko Anniv Vol* 1938:179.
- [25] McClintock FA, Irwin GR. Plasticity aspects of fracture mechanics. *Fract. toughness Test. its Appl.*, Philadelphia, USA: ASTM International; 1965, p. 84–113.
- [26] Novozhilov V V. On a necessary and sufficient criterion for brittle strength. *J Appl Math Mech* 1969;33:201–10.
- [27] Whitney JM, Nuismer RJ. Stress fracture criteria for laminated composites containing stress concentrations. *J Compos Mater* 1974;8:253–65.
- [28] Tanaka K. Engineering formulae for fatigue strength reduction due to crack-like notches. *Int J Fract* 1983;22:39–46. doi:10.1007/BF00942722.
- [29] Lazzarin P, Tovo R, Meneghetti G. Fatigue crack initiation and propagation phases near notches in metals with low notch sensitivity. *Int J Fatigue* 1997;19:647–57.
- [30] Taylor D. Geometrical effects in fatigue: a unifying theoretical model. *Int J Fatigue*

- 1999;21:413–20.
- [31] Taylor D, Wang G. The validation of some methods of notch fatigue analysis. *Fatigue Fract Eng Mater Struct* 2000;23:387–94.
- [32] Susmel L, Taylor D. On the use of the Theory of Critical Distances to predict static failures in ductile metallic materials containing different geometrical features. *Eng Fract Mech* 2008;75:4410–21. doi:10.1016/J.ENGFRACMECH.2008.04.018.
- [33] Madrazo V, Cicero S, Carrascal IA. On the Point Method and the Line Method notch effect predictions in A17075-T651. *Eng Fract Mech* 2012;79:363–79. doi:10.1016/j.engfracmech.2011.11.017.
- [34] Ibáñez-Gutiérrez FT, Cicero S, Carrascal IA, Procopio I. Effect of fibre content and notch radius in the fracture behaviour of short glass fibre reinforced polyamide 6: An approach from the Theory of Critical Distances. *Compos Part B Eng* 2016;94:299–311. doi:10.1016/j.compositesb.2016.03.064.
- [35] Cicero S, Madrazo V, Carrascal IA. Analysis of notch effect in PMMA using the Theory of Critical Distances. *Eng Fract Mech* 2012;86:56–72. doi:10.1016/j.engfracmech.2012.02.015.
- [36] Taylor D. Predicting the fracture strength of ceramic materials using the Theory of Critical Distances. *Eng Fract Mech* 2004;71:2407–16.
- [37] Kasiri S, Taylor D. A critical distance study of stress concentrations in bone. *J Biomech* 2008;41:603–9. doi:10.1016/J.JBIOMECH.2007.10.003.
- [38] Justo J, Castro J, Cicero S, Sánchez-Carro MA, Husillos R. Notch effect on the fracture of several rocks: Application of the Theory of Critical Distances. *Theor Appl Fract Mech* 2017;90:251–8. doi:10.1016/j.tafmec.2017.05.025.
- [39] Susmel L, Taylor D. A novel formulation of the theory of critical distances to estimate lifetime of notched components in the medium-cycle fatigue regime. *Fatigue Fract Eng Mater Struct* 2007;30:567–81. doi:10.1111/j.1460-2695.2007.01122.x.
- [40] Taylor D. A mechanistic approach to critical-distance methods in notch fatigue. *Fatigue Fract Eng Mater Struct* 2001;24:215–24. doi:10.1046/j.1460-2695.2001.00401.x.
- [41] Taylor D, Bologna P, Bel Knani K. Prediction of fatigue failure location on a component using a critical distance method. *Int J Fatigue* 2000;22:735–42. doi:10.1016/S0142-1123(00)00062-1.
- [42] Creager M, Paris PC. Elastic field equations for blunt cracks with reference to stress corrosion cracking. *Int J Fract Mech* 1967;3:247–52. doi:10.1007/BF00182890.
- [43] Hamilton JM. The challenges of deep-water arctic development. *Int J Offshore Polar Eng* 2011;21:241–7.
- [44] Shipilov S, Jones R, Olive J-M, Rebak R. *Environment-Induced Cracking of Materials*. Amsterdam: Elsevier; 2008.
- [45] Specification API. 5LD-2009: Specification for CRA Clad or Lined Steel Pipe.(2009). Am Pet Institute, March n.d.
- [46] BS EN 10225:2009, Weldable Structural Steels for Fixed Offshore Structures Technical Delivery Conditions. 2009.
- [47] Bernstein IM, Pressouyre GM. Role of traps in the microstructural control of hydrogen embrittlement of steels. Pittsburgh: Noyes Publ, Park Ridge, NJ; 1988.
- [48] Arroyo B, Álvarez JA, Lacalle R, Uribe C, García TE, Rodríguez C. Analysis of key factors of hydrogen environmental assisted cracking evaluation by small punch test on medium and high strength steels. *Mater Sci Eng A* 2017;691:180–94. doi:10.1016/j.msea.2017.03.006.
- [49] Alvarez JA, Gutiérrez-Solana F. Elastic-plastic fracture mechanics based methodology to characterize cracking behavior and its application to environmental assisted processes. *Nucl Eng Des* 1999;188:185–202. doi:10.1016/S0029-5493(99)00015-1.
- [50] González P, Cicero S, Álvarez JA, Arroyo B. Analysis of stress corrosion cracking in X80 pipeline steel: An approach from the theory of critical distances. *Procedia Struct Integr* 2018;13:3–10. doi:10.1016/J.PROSTR.2018.12.002.

- [51] ISO 7539 Corrosion of metals and alloys. Stress corrosion testing. Parts 1 to 11. 2015.
- [52] Gangloff RP. Hydrogen assisted cracking of high strength alloys. Charlottesville: Aluminum co of America Alcoa Center PA Alcoa Technical Center; 2003.
- [53] Dietzel W, Srinivasan PB, Atrens A. Testing and evaluation methods for stress corrosion cracking (SCC) in metals. In: Raja VS, Shoji T, editors. *Stress Corros. Crack.*, Woodhead Publishing; 2011, p. 133–66. doi:<https://doi.org/10.1533/9780857093769.2.133>.
- [54] Atrens A, Dietzel W, Srinivasan PB, Winzer N, Kannan MB. Stress corrosion cracking (SCC) of magnesium alloys. In: Raja VS, Shoji T, editors. *Stress Corros. Crack.*, Woodhead Publishing; 2011, p. 341–80. doi:<https://doi.org/10.1533/9780857093769.3.341>.
- [55] Turnbull A. Test methods for environment assisted cracking. *Br Corros J* 1992;27:271–89. doi:[10.1179/bcj.1992.27.4.271](https://doi.org/10.1179/bcj.1992.27.4.271).
- [56] Susmel L, Taylor D. An Elasto-Plastic Reformulation of the Theory of Critical Distances to Estimate Lifetime of Notched Components Failing in the Low/Medium-Cycle Fatigue Regime. *J Eng Mater Technol* 2010;132:021002. doi:[10.1115/1.4000667](https://doi.org/10.1115/1.4000667).
- [57] Cicero S, Madrazo V, García T, Cuervo J, Ruiz E. On the notch effect in load bearing capacity, apparent fracture toughness and fracture mechanisms of polymer PMMA, aluminium alloy A17075-T651 and structural steels S275JR and S355J2. *Eng Fail Anal* 2013;29:108–21. doi:[10.1016/j.engfailanal.2012.11.010](https://doi.org/10.1016/j.engfailanal.2012.11.010).
- [58] Cicero S, García T, Madrazo V, Carrascal IA, Ruiz E. Analysis of notch effect in load bearing capacity, apparent fracture toughness and fracture micromechanisms of ferritic-pearlitic steels. *Eng Fail Anal* 2014;44:250–71. doi:[10.1016/j.engfailanal.2014.05.007](https://doi.org/10.1016/j.engfailanal.2014.05.007).
- [59] Cicero S, Madrazo V, García T. Analysis of notch effect in the apparent fracture toughness and the fracture micromechanisms of ferritic-pearlitic steels operating within their lower shelf. *Eng Fail Anal* 2014;36:322–42. doi:[10.1016/j.engfailanal.2013.10.021](https://doi.org/10.1016/j.engfailanal.2013.10.021).
- [60] Ibáñez-Gutiérrez FT, Cicero S, Carrascal IA. On the influence of moisture content on the fracture behaviour of notched short glass fibre reinforced polyamide 6. *Compos Part B Eng* 2019;159:62–71. doi:[10.1016/j.compositesb.2018.09.062](https://doi.org/10.1016/j.compositesb.2018.09.062).
- [61] Dogan M. Delamination failure of steel single angle sections. *Eng Fail Anal* 2011;18:1800–7. doi:[10.1016/J.ENGFAILANAL.2011.04.009](https://doi.org/10.1016/J.ENGFAILANAL.2011.04.009).
- [62] Martin ML, Fenske JA, Liu GS, Sofronis P, Robertson IM. On the formation and nature of quasi-cleavage fracture surfaces in hydrogen embrittled steels. *Acta Mater* 2011;59:1601–6. doi:[10.1016/j.actamat.2010.11.024](https://doi.org/10.1016/j.actamat.2010.11.024).